

RESOLVED MILLIMETER OBSERVATIONS OF THE HR 8799 DEBRIS DISK

DAVID J. WILNER,¹ MEREDITH A. MACGREGOR,^{1,2,*} SEAN M. ANDREWS,¹ A. MEREDITH HUGHES,³
BRENDA MATTHEWS,⁴ AND KATE SU⁵

¹*Harvard-Smithsonian Center for Astrophysics, 60 Garden Street, Cambridge, MA 02138, USA*

²*Department of Terrestrial Magnetism, Carnegie Institution for Science, 5241 Broad Branch Road, Washington, DC 20015, USA*

³*Department of Astronomy, Van Vleck Observatory, Wesleyan University, 96 Foss Hill Drive, Middletown, CT 06459, USA*

⁴*National Research Council of Canada, Herzberg Astronomy and Astrophysics Programs, 5071 West Saanich Road, Victoria, BC, V9E 2E7, Canada*

⁵*Steward Observatory, University of Arizona, Tucson, AZ 85721, USA*

ABSTRACT

We present 1.3 millimeter observations of the debris disk surrounding the HR 8799 multi-planet system from the Submillimeter Array to complement archival ALMA observations that spatially filtered away the bulk of the emission. The image morphology at 3''8 (150 AU) resolution indicates an optically thin circumstellar belt, which we associate with a population of dust-producing planetesimals within the debris disk. The interferometric visibilities are fit well by an axisymmetric radial power-law model characterized by a broad width, $\Delta R/R \gtrsim 1$. The belt inclination and orientation parameters are consistent with the planet orbital parameters within the mutual uncertainties. The models constrain the radial location of the inner edge of the belt to $R_{\text{in}} = 104_{-12}^{+8}$ AU. In a simple scenario where the chaotic zone of the outermost planet b truncates the planetesimal distribution, this inner edge location translates into a constraint on the planet b mass of $M_{\text{pl}} = 5.8_{-3.1}^{+7.9} M_{\text{Jup}}$. This mass estimate is consistent with infrared observations of the planet luminosity and standard hot-start evolutionary models, with the uncertainties allowing for a range of initial conditions. We also present new 9 millimeter observations of the debris disk from the Very Large Array and determine a millimeter spectral index of 2.41 ± 0.17 . This value is typical of debris disks and indicates a power-law index of the grain size distribution $q = 3.27 \pm 0.10$, close to predictions for a classical collisional cascade.

Keywords: circumstellar matter — stars: individual (HR 8799) — submillimeter: planetary systems

1. INTRODUCTION

The young (30 Myr, Malo et al. 2013) and nearby (39.4 pc, van Leeuwen 2007) A-type star HR 8799 is the host of the first (and so far only) directly imaged multiple planet system. Near-infrared images show four companions with projected separations of 14, 24, 38, and 68 AU (Marois et al. 2008, 2010) whose orbital motions have been tracked over a decade (e.g. see the compilation by Bowler 2016). Comparison of infrared photometry with standard (“hot-start”) evolutionary models suggest these companions have masses in the range of 5 – 10 M_{Jup} (Marley et al. 2012). This inference is consistent with calculations that imply planet masses $< 10 M_{\text{Jup}}$ for dynamical stability at the age of the system, which also could be bolstered by a 1:2:4:8 mean motion resonance configuration (e.g. Goździewski & Migaszewski 2014; Pueyo et al. 2015; Maire et al. 2015). Analysis of self-consistent and homogeneous astrometric measurements indicate that the planet orbits have low eccentricity and are consistent with coplanarity (Konopacky et al. 2016). These relatively bright and wide-separation super-Jovian planets are also a favorite target for spectroscopic observations aimed at planetary atmosphere characterization (Barman et al. 2011; Konopacky et al. 2013; Ingraham et al. 2014; Barman et al. 2015; Bonnefoy et al. 2016; Zurlo et al. 2016).

The HR 8799 system hosts, in addition to planetary mass companions, a dusty debris disk that was first detected by *IRAS* (Sadakane & Nishida 1986). The debris disk has been investigated in detail at wavelengths from 24 – 850 μm using observations from *Spitzer* (Su et al. 2009), *Herschel* (Matthews et al. 2014), and the JCMT (Williams & Andrews 2006; Holland et al. 2017). These multi-wavelength observations show that the debris consists of a warm ($T \sim 150$ K) inner belt and a cold ($T \sim 35$ K) outer belt that bracket the orbits of the directly imaged planets, plus an extended halo of small grains that is detected out to radii beyond 1000 AU. The 850 μm photometry marks the HR 8799 debris disk as one of the most massive known, at an estimated mass of $\sim 0.1 M_{\text{Earth}}$. Modeling of resolved far-infrared images suggests the presence of a population of colliding planetesimals underlying the cold belt that extends from about 100 to 300 AU, albeit with significant uncertainty on the locations of these boundaries on account of insufficient angular resolution for the inner edge and confusion with the extended halo. The relatively large radial extent of this belt coupled with the young age of the system supports “planet-stirring” models to produce the collisional debris (Moór et al. 2015).

Millimeter emission selectively reveals the large dust grains less affected by radiative forces that therefore trace best the distribution of dust-producing planetesimals within debris disks (Wyatt 2006; Wilner et al. 2011). Single dish observations of HR 8799 from the CSO at 350 μm (9" beam) resolved emission from the cold belt around the star, with a tentative offset asymmetry (Patience et al. 2011). This asymmetry was not confirmed by observations with higher signal-to-noise ratio from the JCMT at 450 μm and 850 μm (8" and 13" beam, respectively) (Holland et al. 2017). Millimeter imaging of the disk at much higher angular resolution has proven challenging on account of its low surface brightness. Hughes et al. (2011) made the first millimeter interferometric detection of the disk, using the Submillimeter Array (SMA) at 870 μm , consistent with the presence of a broad belt ($\Delta R/R > 1$) of inner radius ~ 150 AU. Recently, Booth et al. (2016) used the Atacama Large Millimeter/submillimeter Array (ALMA) to image the HR 8799 system at 1.3 mm at much higher sensitivity, although these observations recovered only a small fraction of the total disk emission. Analysis of these ALMA data by an unconventional fitting of belt models to dirty images placed apparently strong constraints on the structure. In particular, their analysis determined an inner edge

too far out to be truncated by the outermost planet b and raised the possibility of the presence of an additional (and unseen) outer planet.

To better determine the properties of the cold belt of planetesimals in the HR 8799 system, we used the SMA to obtain new observations at 1.3 millimeters wavelength that are sensitive to larger angular scales than the previous millimeter interferometer studies by [Hughes et al. \(2011\)](#) and [Booth et al. \(2016\)](#). We also obtained new observations at 9 millimeters wavelength with the Karl G. Jansky Very Large Array (VLA), to constrain the spectral index of the disk emission. In §2, we describe the details of these 1.3 millimeter and 9 millimeter observations. In §3, we present the 1.3 millimeter results in the form of images and deprojected visibility functions, and provide a quantitative analysis of these data using parametric model fits in an MCMC framework. In §4 we discuss implications of the new millimeter results for the system geometry, the mass of planet b, and the grain size distribution. In §5, we summarize the main conclusions.

2. OBSERVATIONS

2.1. *Submillimeter Array*

We observed the HR 8799 system with the SMA on Mauna Kea, Hawaii, at a wavelength near 1.3 millimeters in the subcompact configuration that provides projected baselines as short as 6 meters. Table 1 provides a log of these observations, including the observing dates, weather conditions, number of operational antennas, and the useable hour angle range. In this close-packed antenna configuration, the lower elevation limit for observations is 33° , to prevent antenna collisions. The phase center was set at $\alpha = 23^{\text{h}}07^{\text{m}}28.72$, $\delta = +21^\circ08'03''.3$ (J2000), i.e. the J2000 star position uncorrected for interim proper motion. Two units of the SWARM digital correlator, still under construction at the time, were available; together these spanned bands $\pm(4 - 12)$ GHz from the LO frequency of 225.5 GHz, with uniform channel spacing 140 kHz (~ 0.18 km s $^{-1}$). This setup provided a total of 16 GHz of continuum bandwidth, as well as simultaneous coverage of the ^{12}CO J=2-1 (230.53800 GHz) and ^{13}CO J=2-1 (220.39868 GHz) spectral lines in the upper and lower sidebands, respectively. The primary beam FWHM size of the 6-meter diameter array antennas of $55''(\nu/230$ GHz) set the useable field of view.

The basic observing sequence consisted of a loop of 2 minutes each on the quasars 3C454.3 (~ 13 Jy, 6° away) and J2232+117 (~ 5 Jy, 12° away) and 10 minutes on the target source HR 8799. Passband calibration was obtained with observations of the strong sources 3C454.3 and Uranus. The absolute flux scale was set using observations of Uranus obtained in each track, with 10% overall accuracy. All of the basic calibration was performed using standard procedures in the MIR software package. Continuum visibilities were output in 30 second scans spanning 4 GHz widths, centered at 215.5, 219.5, 231.5, and 235.5 GHz. Fourier inversion for continuum and spectral line imaging and `clean` deconvolution were done in the `CASA` software package (version 4.7.2).

2.2. *Atacama Large Millimeter/submillimeter Array*

We retrieved observations of HR 8799 from the ALMA archive that were made in Band 6 in 2015 January. Details of these observations are described in [Booth et al. \(2016\)](#). We calibrated the five individual scheduling block executions using the associated `CASA` 4.3.1 reduction scripts. In brief, the correlator setup consisted of four spectral windows with width 2 GHz and channel spacing 16 MHz, centered at 216, 218, 231 and 233 GHz, respectively. The observations included baseline lengths from 15 to 349 meters. The primary beam FWHM size of the 12-meter diameter array antennas

Table 1. SMA 1.3 Millimeter Observations of HR 8799

Observation	# of	Projected	τ_{atm}	H.A.
Date	Antennas	Baselines (m)	225 GHz	range
2016 Aug 17	7	7 – 69	0.08	–3.9, +3.7
2016 Aug 27	8	6 – 69	0.08	–4.0, +3.8
2016 Aug 29	8	6 – 69	0.10	–1.7, +3.7
2016 Aug 30	8	6 – 69	0.07	–0.8, +3.7
2016 Sep 06	8	6 – 69	0.09	–3.8, +3.7
2016 Sep 21	7	6 – 45	0.08	–3.6, +3.6

of $27''$ ($\nu/230$ GHz) set the useable field of view. We used the `CASA` task `statwt` to homogenize the visibility weights among scheduling blocks and note that the execution on 2015 January 03 obtained in the best weather conditions dominates the sensitivity budget. Continuum visibilities were output for analysis after flagging the channels with CO line emission, averaging in time to 30 seconds, and averaging in frequency to 2 GHz bandwidth. Imaging was carried out with the `clean` task in `CASA` (version 4.7.2).

2.3. Very Large Array

We observed the HR 8799 system with the VLA at 9 mm wavelength in the most compact D configuration. Observations with the 27 array antennas were executed in 2 hour scheduling blocks on 4 dates in early 2017: Feb 16, Mar 04, 11, and 13. The baselines ranged from 0.04 to 1.03 km. The weather conditions were very good, with phase noise measurements from the Atmospheric Phase Interferometer (on a 300 m baseline at 11.7 GHz) ranging from 3.3 to 7.4°. The phase center was set to the same position as for the SMA observations. The correlator was used to obtain the maximum continuum bandwidth of 8 GHz, comprised of 4 bands centered at 30, 32, 34, and 36 GHz, for two polarizations. The primary beam FWHM size of the 25-meter diameter array antennas is approximately $85''$ ($\nu/30$ GHz). The observing sequence interleaved 1 minute observations of the complex gain calibrator 3C454.3 with 5 minute observations on HR 8799. Passband calibration was obtained with observations of 3C454.3. The absolute flux scale was set with observations of the standard calibrator 3C48 in each execution, with an estimated accuracy of 10%. The basic calibration was done using VLA pipeline processing in the `CASA` package (version 4.7.2) followed by imaging with `clean` task.

3. RESULTS AND ANALYSIS

3.1. Continuum Emission

Figure 1 shows 1.3 mm continuum images of HR 8799 from the SMA (left), ALMA (middle), and the combination of SMA and ALMA (right). These images were obtained with natural weighting, and those including SMA data use a $4''$ FWHM Gaussian taper to improve surface brightness sensitivity at the expense of angular resolution. The ALMA image is comparable to Figure 1 of Booth et al.

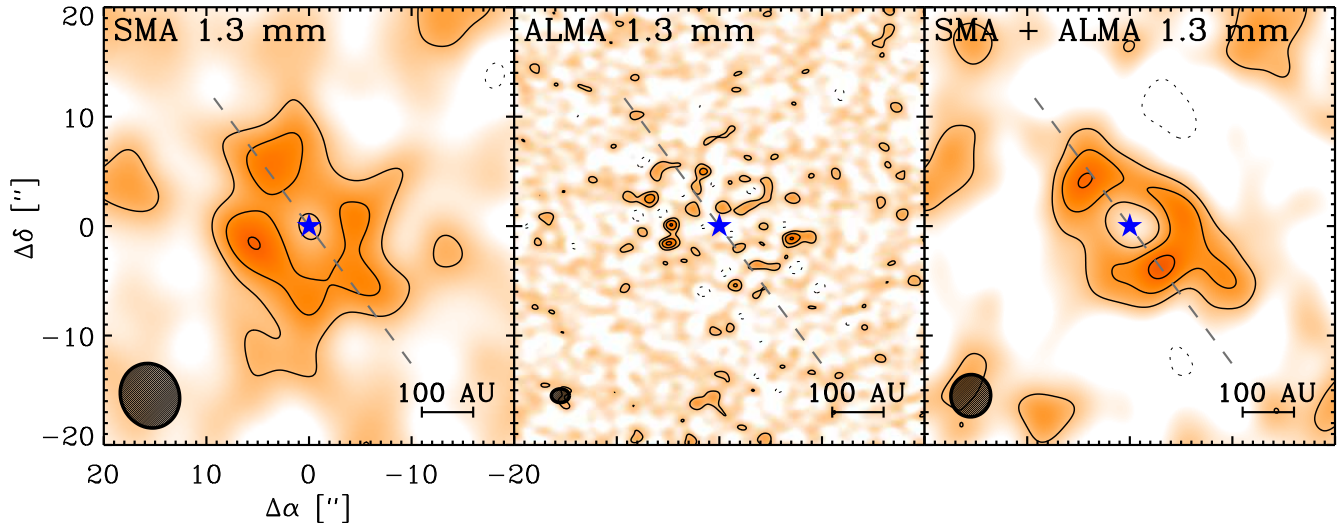


Figure 1. Images of 1.3 mm continuum emission from the HR 8799 debris disk from the SMA (left), ALMA (center), and the SMA and ALMA combined (right). All of these images were made with natural weighting, and those including SMA data make use of a $4''$ FWHM Gaussian taper. Contour levels are in steps of $2\times$ the measured rms values are $180 \mu\text{Jy}/\text{beam}$, $16 \mu\text{Jy}/\text{beam}$, and $30 \mu\text{Jy}/\text{beam}$ for the three images, respectively. The beam sizes are shown by the ellipses in the lower left corner of each image and are $6''.1 \times 5''.6$, $1''.7 \times 1''.2$, and $3''.8 \times 3''.7$, respectively. The blue star symbol indicates the stellar position, and the dashed gray line shows the best-fit belt position angle (see §3.3).

(2016), with a beam size of $\sim 1''.5$, and it shows a noisy ring of emission surrounding the star. For the SMA image, the beam size is $\sim 4\times$ larger in each dimension than for the ALMA image, and the noise level is an order of magnitude higher, but the sensitivity to larger angular scales provided by the shorter baselines enables a much improved representation of the radially extended belt of emission around the star. The combination of SMA and ALMA data results in an even better image of this circumstellar structure. In the SMA and ALMA combined image shown with a $\sim 3''.8$ beam, the two peaks visible on either side of the star are the signatures of limb brightening along the major axis of an inclined and optically thin emission belt.

Figure 2 shows the deprojected visibility function for the emission from the SMA and ALMA, obtained by averaging the real and imaginary parts of the complex visibilities in concentric annular bins, adopting the belt geometry derived in §3.3. This view of the visibilities provides some insight into the image properties in Figure 1. The shorter baselines from the SMA capture the steep rise in visibility amplitude at low spatial frequencies that are missed by ALMA, and thus sample better the emission responsible for the extended disk morphology. The visibilities from the two telescopes are consistent where they overlap at higher spatial frequencies that sample the small scale structure. The imaginary parts of visibilities are all consistent with zero, as expected for an axisymmetric structure.

Figure 3 shows a VLA 9 millimeter continuum image of the HR 8799 system, obtained with natural weighting and a $5''$ FWHM Gaussian taper, which gives a beam size of $6''.2 \times 5''.8$ and rms noise of $4.3 \mu\text{Jy}/\text{beam}$. Significant emission is detected from an extended region centered on the star, but with a low peak signal-to-noise ratio of only 3 – 4 per beam. No clear disk or belt morphology is

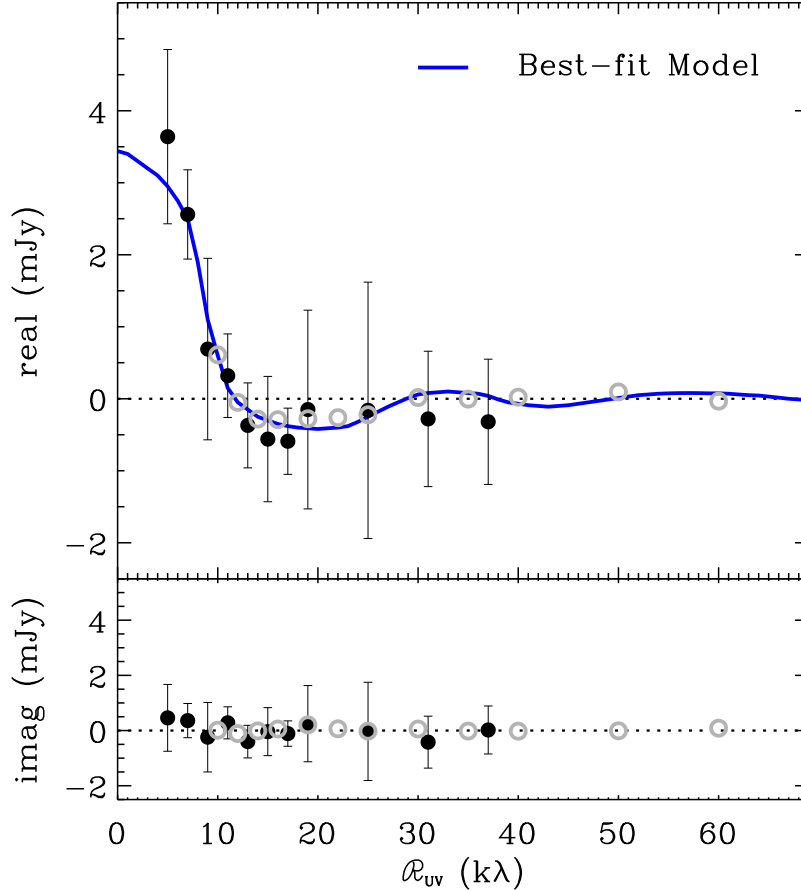


Figure 2. The real and imaginary parts of the 1.3 mm visibilities, averaged in bins of deprojected (u, v) distance from the star, for data from the SMA (black filled circles) and ALMA (gray open circles). The solid blue line depicts the best-fit power law axisymmetric belt model to the combined dataset (see §3.3). The imaginaries are consistent with zero as is expected for an axisymmetric belt.

evident in the emission at this sensitivity level. The emission peak near $(+10'', -10'')$ in the image could be the result of a noise fluctuation, or perhaps a faint and unrelated background source.

3.2. Line Emission

Emission from the ^{12}CO and ^{13}CO J=2-1 lines were clearly detected by the SMA observations over the narrow v_{LSR} range -6 to -4 km s^{-1} , close to the stellar velocity of -4.6 km s^{-1} in this reference frame. Single dish observations of the ^{12}CO J=3-2 line with a $15''$ beam show extended emission, concentrated in a filament that extends from the north-northeast of HR 8799 to the south-southwest, most likely affiliated with the nearby MBM 53-55 complex of high latitude clouds (Williams & Andrews 2006; Su et al. 2009). The submillimeter dust continuum emission observed by *Herschel* also shows traces of this large scale feature (Matthews et al. 2014). Like previous attempts to use interferometers to image the molecular emission in this region, the extended structure evident in lower angular resolution single dish maps (Su et al. 2009) remains poorly sampled and highly problematic to reconstruct, even with the lower spatial frequency information newly obtained

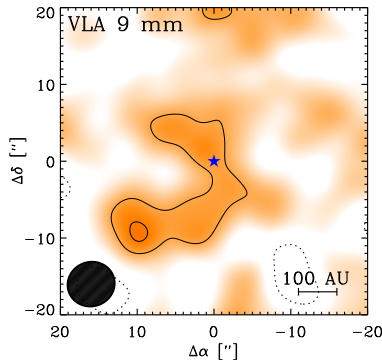


Figure 3. Image of the 9 millimeter continuum emission from the HR 8799 debris disk from the VLA obtained with natural weighting and a $5''$ FWHM Gaussian taper. Contour levels are $\pm 3, 5 \times$ the measured rms of $4.3 \mu\text{Jy}/\text{beam}$. The $6''.2 \times 5''.8$ beam size is indicated by the ellipses in the lower left corner and the stellar position by the blue star symbol.

with the SMA. Regardless of the choice of visibility weighting scheme and clean deconvolution parameters, all of our attempts at imaging the line emission show pronounced artifacts. Emission from the ^{13}CO $J=2-1$ line, with substantially lower optical depth than the main isotopologue, offers the best chance to reveal structure associated with the HR 8799 system. Figure 4 shows a set of ^{13}CO channel maps obtained with natural weighting and a $4''$ FWHM Gaussian taper, resulting in a $\sim 6''.5$ beam. Among the positive and negative corrugations indicative of missing flux, the most significant emission is located away from the star, and there is no clear evidence for any systematic motions that might be associated with rotation of gas in the debris disk. The linewidth is consistent with the typical turbulent broadening found in small molecular clouds. The apparent association in space and velocity between HR 8799 and this extended molecular emission is intriguing but remains mysterious.

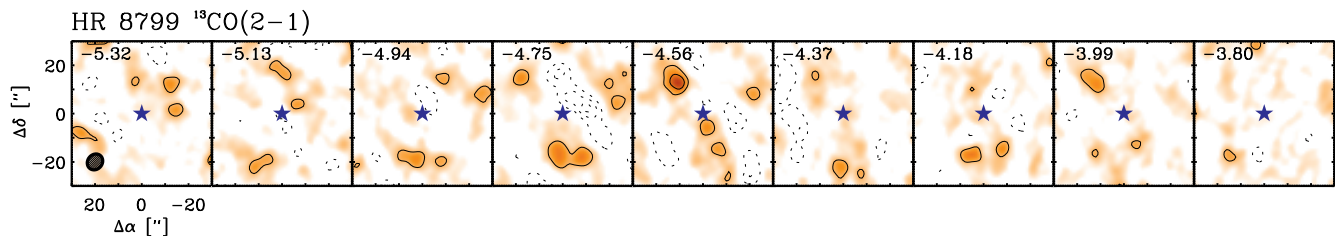


Figure 4. SMA channel maps of ^{13}CO $J = 2 - 1$ emission for HR 8799. For all panel, the contours are in steps of $\pm 2 \times$ the rms noise level of $100 \text{ mJy}/\text{beam}$. The ellipse in the lower left corner of the leftmost panel indicates the $7''.0 \times 6''.1$ synthesized beam size resulting from natural weighting and a $4''$ Gaussian taper. The LSR velocities are labeled in the upper left corner of each panel.

3.3. SMA/ALMA Disk Model Fits

To provide a quantitative characterization of the 1.3 millimeter emission from the HR 8799 disk, we make the simple assumption that the structure can be represented by an axisymmetric and geometrically thin belt, and we model the observations using the visibility fitting procedure described in MacGregor et al. (2013). The surface brightness of the belt is assumed to be a radial power law,

$I_\nu \propto r^x$, between an inner and outer radius, R_{in} and R_{out} , respectively. The surface brightness power law index, x , encapsulates both the radial surface density and temperature profiles of the emitting grains. The total flux density of the belt is normalized to $F_{\text{belt}} = \int I_\nu d\Omega$. We also fit for the belt geometry, specifically an inclination, i (where 0° is face-on), and a position angle, PA (measured East from North). For comparison with observed visibilities, the model emission is multiplied by the appropriate primary beam response of each telescope. Since imaging with both *Herschel* (Matthews et al. 2014) and JCMT (Holland et al. 2017) shows the presence of a compact background source to the northwest of the disk, we also include an unresolved point source at this location in the model, described by a total flux, F_{pt} , and an offset from the phase center of the observations, $\{\Delta\alpha_{\text{pt}}, \Delta\delta_{\text{pt}}\}$. When modeling the ALMA data alone, this additional background source is omitted on account of primary beam attenuation at the offset location.

This simple two-dimensional parametric model for the disk emission is incorporated into a Markov Chain Monte Carlo (MCMC) framework. For each model image, we calculate synthetic visibilities using `vis_sample`¹, a python package for visibility sampling that improves on the sampling and interpolation of the `uvmodel` task in the Miriad software package, and determine a χ^2 likelihood function, $\ln\mathcal{L} = -\chi^2/2$, that incorporates the statistical weights of the visibilities. We make use of the `emcee` package (Foreman-Mackey et al. 2013) to sample the posterior probability distribution of the data conditioned on the model, and determine the best-fit parameter values and their uncertainties. We explore the posterior with 50,000 iterations (100 walkers and 5,000 steps each) and check that the Gelman-Rubin statistic (Gelman et al. 2014) is $\hat{R} < 1.1$ for all parameters to ensure convergence.

We first fit the SMA observations and the ALMA observations separately, to examine the constraints provided by each dataset alone, and then fit the observations from both telescopes simultaneously, to examine the joint constraints. Table 2 lists the best-fit parameters from each of these fits, together with their 68% uncertainties determined from the marginalized posterior probability distributions. For modeling the SMA observations alone, we adopt uniform priors for all parameters, in particular $0 < R_{\text{in}} < R_{\text{out}}$, $F_{\text{belt}} > 0$, and $-3 < x < 3$. When modeling the ALMA observations alone, informative constraints were not obtained for the outer radius or total flux parameters using these assumptions. In effect, the ALMA data allow the outer radius parameter to extend freely, with ever increasing total flux. This most likely results because the ALMA primary beam is comparable in size to the HR 8799 emission region, and the ALMA observations provide very little data at spatial frequencies inside the first null of the visibility function to limit the total disk emission. To obtain constraints on these parameters from the ALMA data alone, we must impose strong priors on both R_{out} and F_{tot} . As an example, we implemented a Gaussian prior on the total belt flux density, $3.0 \leq F_{\text{tot}} \leq 4.0$ mJy, motivated by submillimeter observations (Matthews et al. 2014) that predict a flux density of ~ 3.5 mJy at 1.3 mm assuming a millimeter spectral index of 2.5, typical of debris disks (MacGregor et al. 2016). We note that the fit to the SMA data alone yields a higher flux density of $5.13_{-1.01}^{+0.34}$ mJy, but still comparable within the uncertainties. In addition, we implemented a logistic function $f(x) = 1/(1 + e^{-k(x-x_0)})$ prior for the outer radius with $k = -10$ and $x_0 = 512$ AU, the primary beam diameter. With these assumptions, fitting the ALMA observations alone yields $F_{\text{tot}} = 3.5 \pm 0.5$ mJy and $R_{\text{out}} = 497.(+2., -150)$ AU, effectively recovering the priors. We suspect that the $\sim 10\%$ uncertainties on the disk parameters quoted by Booth et al. (2016)

¹ `vis_sample` is publicly available at https://github.com/AstroChem/vis_sample or in the Anaconda Cloud at https://anaconda.org/rloomis/vis_sample

from an image-based analysis of the ALMA observations are underestimated, perhaps in part due to unaccounted covariance associated with large scale emission. By contrast, modeling the SMA and ALMA observations simultaneously does not require strong priors on the disk parameters to obtain meaningful constraints. Figure 5 shows the posterior probability distributions for the model parameters that result from fitting the SMA and ALMA observations together. For these combined fits, the small proper motion of HR 8799 between SMA and ALMA observing epochs ($0''.20$) was ignored, given its insignificance at the low angular resolution of the SMA observations.

Figure 6 shows the combined SMA and ALMA image from Figure 1 together with images of the best-fit model at full resolution, the best-fit model imaged in the same way as the data, and an image made from the observed visibilities after subtracting the best-fit model visibilities. This broad ($\Delta R/R \gtrsim 1$) inclined belt model reproduces very well the main features of the observations, including the inner depression and limb-brightened regions in the northeast and southwest. The goodness-of-fit is demonstrated by the noise-like residual image. Notably, the imaged residuals reveal no significant azimuthal brightness asymmetries, as might arise from the presence of resonant clumps, or an offset of the star from the center of the disk. If any such asymmetries are present in the millimeter emission from the HR 8799 disk, observations with a significantly higher signal-to-noise ratio will be required to reveal them. This outer belt of large fractional width joins a growing list of other young debris disks with similar characteristics, e.g. HD 95086 (Su et al. 2017), that are much broader than the classical Kuiper Belt of our Solar System (especially the low excitation “kernel” component discussed by Bannister et al. 2016).

3.4. VLA 9 millimeter Flux Estimate

In the VLA image, the disk is detected only at the $\sim 3\sigma$ per beam level, and we do not apply the same MCMC modeling technique to these data. For simplicity, we measure the flux density in CASA within a circular aperture centered at the location of the disk, assuming the diameter of the disk determined from the combined modeling of the SMA and ALMA data. We determine the uncertainty by measuring the flux density in the same circular aperture at ten random locations in the image and taking the average. The measured total flux density of the disk from our VLA observations is $F_{9\text{mm}} = 32.6 \pm 9.9 \mu\text{Jy}$ (correction for primary beam attenuation is negligible). We adopt this image-based approach instead of fitting to the millimeter visibilities due to the difficulty in selecting a function that adequately reproduces the complex structure of the observed surface brightness profile.

4. DISCUSSION

By modeling new and archival resolved millimeter observations, we have made an improved characterization of the planetesimal belt within the debris disk surrounding the HR 8799 planetary system. This broad emission belt spans from ~ 100 – 360 AU, roughly consistent with previous modeling of the spectral energy distribution (Su et al. 2009) and fitting far-infrared emission images (Matthews et al. 2014). The 1.3 millimeter interferometric dataset from SMA and ALMA together recovers the bulk of the disk flux and provides high angular resolution, and we used this combined dataset to fit for basic structural parameters. We next consider implications. In particular, we examine the belt geometry constraints in the context of coplanarity and alignment of the planetary system (§4.1), the relationship between the belt inner edge and the outermost planet b (§4.2), ramifications of the radial

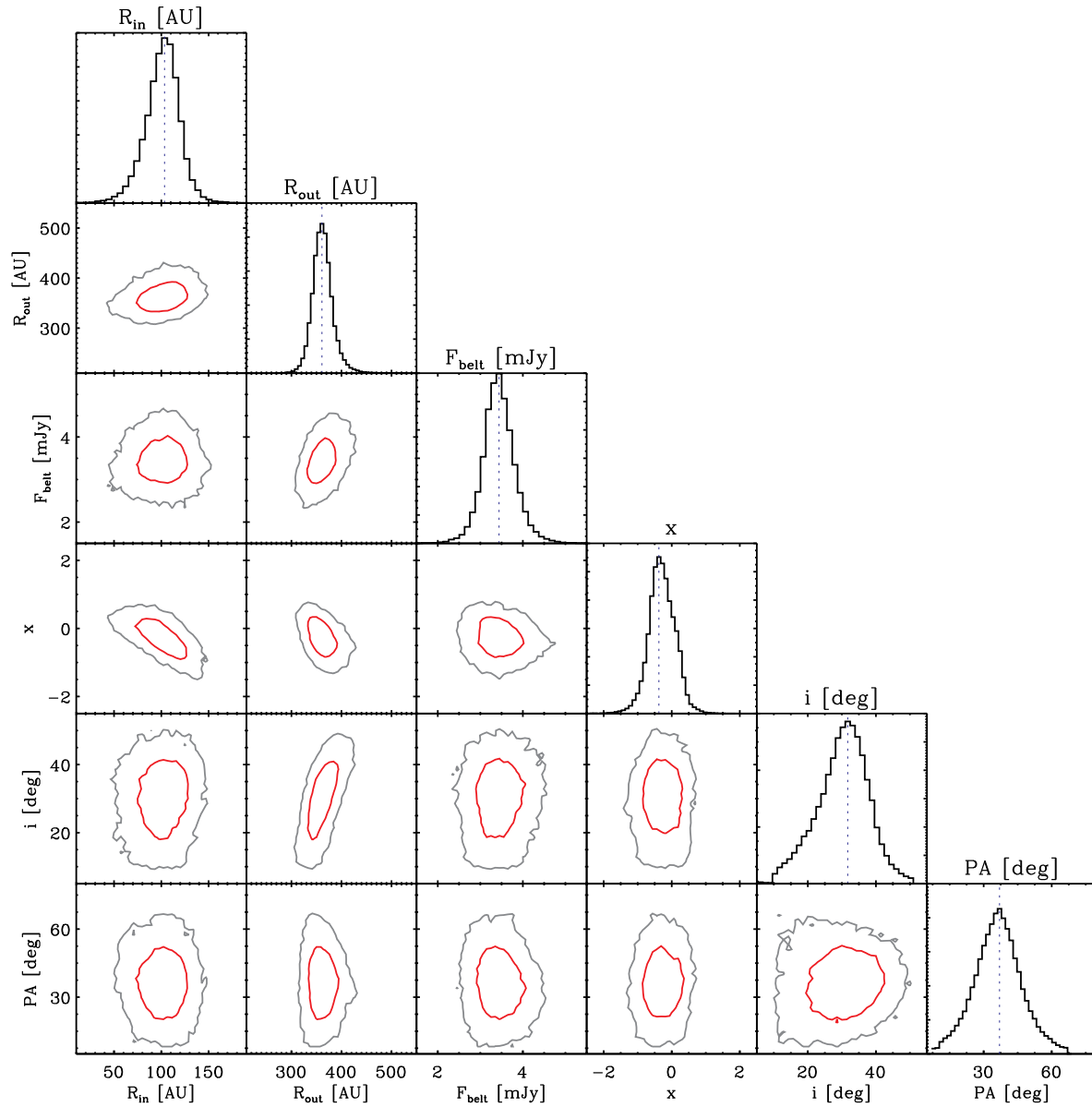


Figure 5. Corner plot summary of parameter values from the MCMC belt modeling of the combined SMA and ALMA data. The panels on the diagonal show the 1-D histogram for each model parameter obtained by marginalizing over the other parameters, with a dashed vertical line to indicate the best-fit value. The off-diagonal panels show 2-D projections of the posterior probability distributions for each pair of parameters, with contours to indicate 1σ (red) and 2σ (grey) regions.

surface density profile for collisional excitation mechanisms (§4.3), and the millimeter spectral index connections to debris disk collisional models (§4.4).

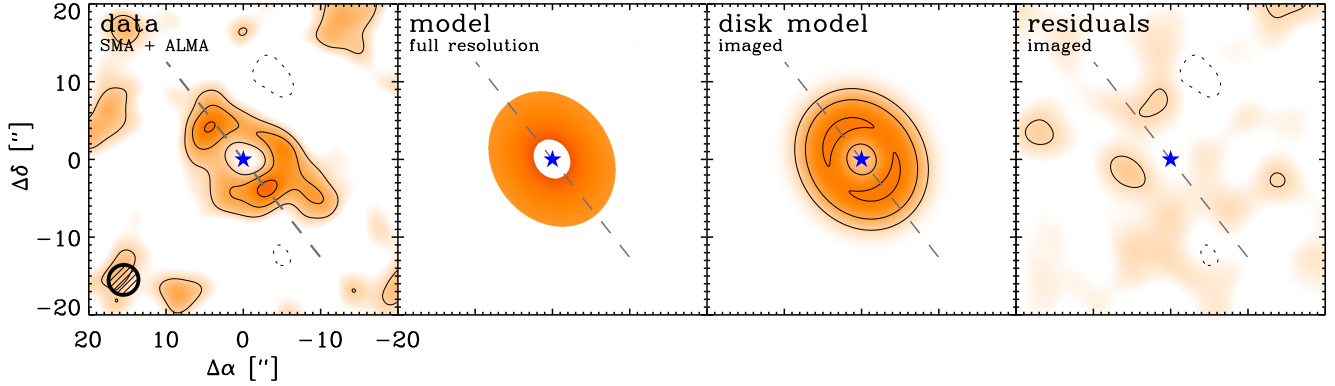


Figure 6. (left) The combined SMA and ALMA image of the HR 8799 debris disk. (center left) The best-fit model to the combined datasets displayed at full resolution (pixel size $0''.5 = 2$ AU at 39.4 pc). (center right) The best-fit combined model convolved with the synthesized beam. (right) The residuals obtained from imaging the best-fit model subtracted from the data. In all panels except the full resolution model, contours are in steps of $2 \times 30 \mu\text{Jy}/\text{beam}$, the rms noise level. The blue star marks the stellar position, the dashed gray line indicates the best-fit position angle of the disk, and the dashed gray ellipse in the leftmost panel shows the $3''.8 \times 3''.7$ synthesized beam.

Table 2. Best-fit Model Parameters

Parameter	Description	SMA	ALMA ^a	SMA+ALMA
F_{belt}	Total belt flux density [mJy]	5.13(+0.34, -1.01)	3.50 ± 0.50	3.44(+0.31, -0.56)
R_{in}	Belt inner edge [AU]	106.(+19., -28.)	115.(+16., -17.)	104.(+8., -12.)
R_{out}	Belt outer edge [AU]	370.(+42., -40.)	497.(+22., -150.)	361.(+16., -18.)
x	Surface brightness power law index	-0.56(+0.31, -0.83)	-0.64(+0.40, -0.46)	-0.38(+0.47, -0.47)
i	Disk inclination [°]	35.6(+5.6, -4.4)	34.3(+5.9, -6.9)	32.8(+5.6, -9.6)
PA	Disk position angle [°]	41.6(+9.6, -7.8)	43.7(+12.2, -12.4)	35.6(+9.4, -10.1)
F_{pt}	background source flux density [mJy]	0.47(+0.11, -0.17)	...	0.45(+0.12, -0.15)
$\Delta\alpha_{\text{pt}}$	background source RA offset ["]	-12.9(+0.2, -0.9)	...	-12.2(+0.8, -0.8)
$\Delta\delta_{\text{pt}}$	background source DEC offset ["]	17.8(+0.4, -0.6)	...	17.5(+0.9, -0.5)

^aAdopting strong priors on the total belt flux density and belt outer edge parameters (see §3.3).

4.1. System Geometry

The model fits to the millimeter emission provide new estimates of the inclination and orientation of the planetesimal belt that can be compared directly to constraints on the orbital elements of the planets. Formation of planets in a thin disk will generally lead to orbital coplanarity and alignment, unless upset by dynamical events. Since the orbital periods of the HR 8799 outer planets span centuries, only small arcs of their motions around the star have been measured in the years since discovery, leaving significant uncertainties in their orbital elements. Early stability calculations indicated departures from a face-on geometry (Fabrycky & Murray-Clay 2010), and most analyses have favored orbits with inclinations of 10 to 30° (e.g. Currie et al. 2012; Esposito et al. 2013;

Pueyo et al. 2015; Wertz et al. 2017). A recent analysis of carefully calibrated astrometric monitoring data that minimizes systematic errors generally indicate more highly inclined orbits, specifically $38^\circ \pm 7^\circ$ for the outermost planet b, and no evidence for any measureable departures from coplanarity (Konopacky et al. 2016). Astroseismology suggests a higher inclination angle for the star, $\gtrsim 40^\circ$, as well (Wright et al. 2011). These results are all compatible with the disk inclination of $32^\circ 8_{-9.6}^{+5.6}$ derived from the combined SMA and ALMA data.

There is some tension between the millimeter result and the lower (and more precise) disk inclination of $26^\circ \pm 3^\circ$ determined from the ellipticity of the outer edge of far-infrared emission in *Herschel* images (Matthews et al. 2014). As noted by Booth et al. (2016), the discrepancy between millimeter and far-infrared disk inclinations may have a physical origin in size-dependent dust dynamics, or in complexities in disk structure not captured by the simple belt models. Taking the millimeter emission as the best tracer of the dust-producing planetesimals, the various inclination determinations are compatible with coplanarity with the planetary orbits, and with the star, although the uncertainties remain large enough to preclude drawing a firm conclusion.

If the planetesimal belt and planet orbits are coplanar, as suggested by the derived inclination angle, then we would also expect alignment of the position angle of the belt and the argument of ascending node of the planet orbits, Ω . The Konopacky et al. (2016) astrometric analysis indicates Ω lies in the range of 40 to 70° for low eccentricity solutions, for all four of the planets. The disk position angle of $35^\circ 6_{-10.1}^{+9.4}$ determined from the joint analysis of the SMA and ALMA data is compatible with the low end of this range. Like the inclination, the disk position angles derived from millimeter and far-infrared emission are discrepant, with the latter yielding a higher value of $64^\circ \pm 3^\circ$ (Matthews et al. 2014). Again, there may be a physical origin for this difference. The overlap of the millimeter constraint on the planetesimal belt position angle and the planetary argument of ascending node provides weak additional support for coalignment of these components.

4.2. Dynamical Constraints on the Mass of Planet b

Because the wide-separation HR 8799 planets are relatively accessible to optical and near-infrared observations, they have become key benchmark objects for models of planetary atmospheres and evolution. Evolutionary models are highly degenerate in planet mass, luminosity and age, however, in part because the imprint of initial conditions can persist for 100’s of Myr (Marley et al. 2007). Depending on initial thermal content, giant planets can exhibit a wide range of luminosities. In principle, independent constraints on planet mass from dynamics offer the potential to break these model degeneracies. Such constraints have the potential to help distinguish between planet formation models, in particular hot-start models where most entropy is retained, e.g. by gas that collapses directly to form planets, from cold-start models where most entropy is lost, e.g. by gas cooling in core accretion. Notably, the core accretion mechanism is challenged to form $5 - 10 M_{\text{Jup}}$ planets *in situ* at the large orbital radii of the HR 8799 planets (Kratte et al. 2010). The observed luminosities of the HR 8799 planets cannot be reproduced by the most extreme cold-start models proposed by Marley et al. (2007). However, they are compatible with the intermediate “warm-start” models discussed by Spiegel & Burrows (2012) and Marleau & Cumming (2014), since luminosity increases with both mass and initial entropy (for a given age). These models would imply much higher planet masses than hot-start models by up to a factor of two (or perhaps more). For planet b, a fully self-consistent solution for the planet properties remains elusive once spectroscopic constraints are combined with infrared photometry, likely due to limitations of the models (Marley et al. 2012).

Dynamical constraints on planet masses would be valuable, but they are generally difficult to obtain for wide-separation planets that are impractical to monitor over many orbital periods.

For HR 8799, analysis of the long-term stability of the system offers one form of dynamical mass constraint on the planets. The HR 8799 multi-planet system was investigated numerically by [Götberg et al. \(2016\)](#) who found that nominal models with 5–7 M_{Jup} planets are unstable on timescales much shorter than the system age. One natural solution to this problem is if the planet masses are substantially lower than estimated from infrared observations. Lower mass planets have larger separations in terms of Hill radii, and the system stability persists for much longer times. If standard cooling models underpredict the planet luminosities, as some calculations suggest (e.g. [Mordasini 2013](#)), then lower planet masses – more like 2–3 M_{Jup} – might be accommodated. Alternatively, much higher planet masses can be viable if the orbits are stabilized by resonant lock. The configuration of the HR 8799 planet orbits appear to be consistent with a 1:2:4:8 resonance (e.g. [Reidemeister et al. 2009](#); [Konopacky et al. 2016](#)).

The truncation of the inner edge of the planetesimal disk by the gravity of the outermost planet b offers another form of dynamical mass constraint. The separation of the planet from the disk is sensitive to the planet mass, as the planet clears a chaotic zone around itself due to resonance overlap (e.g. [Quillen 2006](#); [Chiang et al. 2009](#)). For the simple case of circular and coplanar orbits, [Wisdom \(1980\)](#) derived an analytic formula for the width of the chaotic zone exterior to the planetary orbit, $\Delta a = C a_{\text{pl}} (M_{\text{pl}}/M_*)^{2/7}$, where C is a scaling coefficient of 1.3, a_{pl} is the semi-major axis of the planet, and M_{pl} and M_* are the mass of the planet and the star, respectively. Other work that adopts a slightly different definition of resonance width gives a different scaling factor (e.g. 1.4, [Malhotra 1998](#)). The width of the chaotic zone for more complex configurations has been the subject of numerous investigations, considering additional factors like the eccentricity of the planet orbit ([Quillen & Faber 2006](#); [Regaly et al. 2017](#)), and eccentricities of the planetesimal orbits with the disk ([Mustill & Wyatt 2012](#); [Pearce & Wyatt 2014](#)). The [Pearce & Wyatt \(2014\)](#) study formulates a convenient expression for the location of the disk inner edge relative to the width of the chaotic zone, $R_{\text{in}} = a_{\text{pl}} + 5a_{\text{pl}}(M_{\text{pl}}/3M_*)^{1/3}$, taken in the limit of zero eccentricity.

If we adopt the [Pearce & Wyatt \(2014\)](#) formula, then we can translate the radial location of the inner edge of the millimeter belt, $R_{\text{in}} = 104_{-12}^{+8}$ AU, directly into a constraint on the mass of the outermost planet b. [Figure 7](#) shows the result of this translation of the inner radius posterior distribution from our modeling, assuming planet b truncates the belt. For this calculation, we adopt the planet semi-major axis $a_{\text{pl}} = 68$ AU and stellar mass $M_* = 1.56 M_{\odot}$ from dynamical analysis ([Soummer et al. 2011](#)), consistent with optical photometry and spectral synthesis ([Gray & Kaye 1999](#)). This procedure gives $M_{\text{pl}} = 5.8_{-3.1}^{+7.9} M_{\text{Jup}}$ for the planet b mass, compatible with standard planet cooling models, though the errors are still large enough to encompass both hot-start and a range of warm-start initial conditions. This new determination improves on previous attempts that use an inner belt radius estimated from the spectral energy distribution ([Su et al. 2009](#)), or from the ALMA data alone ([Booth et al. 2016](#)), both of which suffer from substantial systematic uncertainty. Given this result, there is no need to posit the presence of an additional unseen planet orbiting beyond planet b, or variations in the orbit of planet b, to account for the disk truncation. Since this planet mass constraint scales very steeply with the disk-planet separation, even a modest improvement in the constraint on the radial location of the inner edge of the millimeter belt has the potential to significantly reduce the uncertainty on the planet b mass estimate. Deeper observations of HR 8799

could be readily obtained with the SMA, or the Atacama Compact Array (ACA), at the appropriate spatial frequencies, to improve the constraint. A better planet b mass estimate obtained in this way could provide important feedback into the system dynamics, planet cooling models, and formation scenarios.

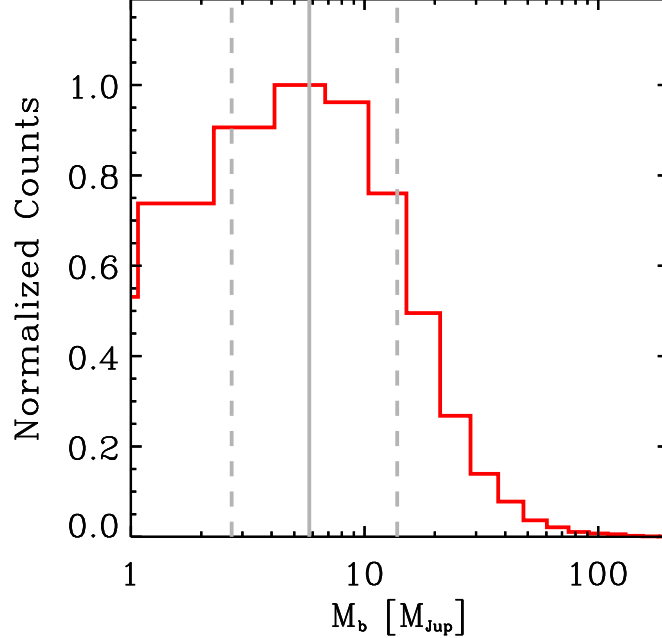


Figure 7. Constraint on the mass of planet b obtained by assuming this planet truncates the inner edge of the HR 8799 millimeter belt. To generate this figure, we have translated the inner radius posterior distribution from our MCMC modeling of the millimeter emission shown in Figure 5. The solid gray line indicates the best-fit results, and the dashed gray lines indicate the 1σ uncertainties.

4.3. *Stirring Mechanisms*

The planetesimals within debris disks like HR 8799 must be “stirred” in order to incite destructive collisions (Wyatt 2008). The two leading mechanisms are self-stirring by an outwardly moving front of planetoid formation and growth (Kenyon & Bromley 2002) and planet-stirring by the gravitational influence of interior giant planets (Mustill & Wyatt 2009). Given the young age of HR 8799, Moór et al. (2015) concluded that the disk is most likely planet-stirred, since the long timescales needed to form Pluto-sized bodies at 100’s of AU are not compatible with the large extent of the disk that is inferred from far-infrared imaging. The extent of the planetesimal belt more directly traced by millimeter emission supports this conclusion. Moreover, it seems likely that the giant planets responsible for stirring the debris disk are detected directly.

An additional observable that may help to discriminate between stirring scenarios is the radial distribution of planetesimals. Self-stirred models produce an extended planetesimal disk with an outwardly increasing surface density (e.g., $\Sigma \propto r^{+7/3}$ in the models of Kennedy & Wyatt 2010). By contrast, standard steady-state debris disk models tend to produce surface density gradients that decrease with radius (e.g. Krivov et al. 2006). High quality resolved millimeter observations of a

handful of debris disks suggest either rising surface density profiles (MacGregor et al. 2015) or hint at more complex radial structures (e.g. multiple cold belts in HD 107146, Ricci et al. 2015). From our model fits for HR 8799, the best-fit power law index for the millimeter emission radial profile is $x = -0.38 \pm 0.47$. If we assume a radial temperature profile $T(r) \propto r^{-0.5}$ to approximate radiative equilibrium with stellar heating, then this implies a surface density profile $\Sigma(r) \propto r^{0.12 \pm 0.47}$. While the uncertainties are still significant, this best-fit shallow dependence of planetesimal surface density on radius is not predicted in self-stirring scenarios. This result also favors planet-stirring as the basic collisional excitation mechanism for this radially extended debris disk.

4.4. Grain Size Distribution

The spectral index of dust emission at millimeter wavelengths from debris disks encodes information on the grain size distribution that can be used to assess collisional models (Ricci et al. 2012). For a power law grain size distribution, $n(a) \propto a^{-q}$, the reference model is the classical steady state collisional cascade where $q = 7/2$ (Dohnanyi 1969). Lower or higher values of q may be obtained by varying the strength and velocities of colliding bodies (Pan & Sari 2005; Pan & Schlichting 2012), and are found in time-dependent numerical models of debris disk evolution (e.g. Schüppler et al. 2015).

For HR 8799, we use the best-fit total flux density from the combined SMA and ALMA models at 1.3 millimeters and the VLA flux density measured at 9 millimeters to obtain a millimeter spectral index of $\alpha_{\text{mm}} = 2.41 \pm 0.17$. Given a grain composition model, α_{mm} provides a constraint on the size distribution of the emitting grains, in particular on the power-law index $q = (\alpha_{\text{mm}} - \alpha_{\text{P1}})/\beta_s + 3$. In this expression, valid for $3 < q < 4$, β_s is the dust opacity power law index in the small grain limit, 1.8 ± 0.2 for interstellar grain materials (Draine 2006), and α_{P1} is the spectral index of the Planck function, 1.92 ± 0.10 (the Rayleigh-Jeans limit modified by a small correction factor from the 39.7 K dust temperature assumed for HR 8799). Given the measured millimeter fluxes for HR 8799, the resulting grain size distribution power-law index is $q = 3.27 \pm 0.10$. This result is consistent with the weighted mean value of $q = 3.36 \pm 0.02$ determined by MacGregor et al. (2016) for a sample of 15 debris disks observed over a similar wavelength range. This grain size distribution is most consistent with a classical collisional cascade, with no need to invoke additional complexities in the collisional model.

5. CONCLUSIONS

We have made new observations of millimeter dust continuum emission from the debris disk that surrounds the four directly imaged planets in the HR 8799 system. SMA observations at 1.3 millimeters complement archival ALMA observations by adding measurements at lower spatial frequencies to better sample extended emission. By fitting simple parametric disk models to these data in an MCMC framework, we obtain constraints on the structural parameters of the millimeter emission. The main conclusions from this analysis are:

1. The 1.3 mm emission morphology imaged at $3''8$ (150 AU) resolution is consistent with a broad ($\Delta R/R \gtrsim 1$), axisymmetric, inclined belt centered on the star. These data provide no evidence for the presence of clumps or other azimuthal asymmetries that would betray dynamical sculpting of the disk by the gravity of the interior orbiting planets.

2. Model fits to the combined SMA and ALMA visibilities constrain the millimeter belt inclination, $32^{\circ}8_{-9.6}^{+5.6}$, and position angle, $35^{\circ}6_{-10.1}^{+9.4}$. These values overlap with estimates of the orbital inclination and angle of ascending node of the planet orbits determined by astrometric observations, and they are consistent with a coplanar configuration of the disk and planetary orbits within the (still large) mutual uncertainties.
3. The best-fit inner edge of the millimeter emission belt, $R_{\text{in}} = 104_{-12}^{+8}$ AU, provides an independent dynamical constraint on the mass of the outermost planet b of $5.8_{-3.1}^{+7.9}$ M_{Jup} under the assumption that the chaotic zone of this planet truncates the planetesimal disk. This dynamical mass estimate is commensurate with those obtained from the planet luminosity and standard hot-start evolutionary models, although the uncertainties allow for a range of initial thermal content.
4. Flux density measurements at 1.3 and 9 millimeters from the SMA and VLA, respectively, give a spectral index of 2.41 ± 0.17 , which implies a grain size distribution power-law index of $q = 3.27 \pm 0.10$. This value is consistent with the weighted mean value of q determined from millimeter observations of other debris disks and close to predictions for a steady state collisional cascade.

The millimeter observations presented here have improved our view of the large scale spatial distribution of the dust-producing bodies in the debris disk surrounding the HR 8799 planetary system. However, these observations still lack the sensitivity needed to reveal any details of planet-disk interactions, or to obtain dynamical constraints on planet mass that usefully discriminate between planet evolutionary models. Deeper millimeter observations should be pursued to obtain better constraints on the planetesimal belt morphology, and to determine if more a sophisticated approach is needed for modeling and interpretation.

M.A.M. acknowledges support from the National Science Foundation under Award No. 1701406. The Submillimeter Array is a joint project between the Smithsonian Astrophysical Observatory and the Academia Sinica Institute of Astronomy and Astrophysics and is funded by the Smithsonian Institution and the Academia Sinica. This paper makes use of the following ALMA data: ADS/JAO.ALMA#2012.1.00482.S. ALMA is a partnership of ESO (representing its member states), NSF (USA) and NINS (Japan), together with NRC (Canada), MOST and ASIAA (Taiwan), and KASI (Republic of Korea), in cooperation with the Republic of Chile. The Joint ALMA Observatory is operated by ESO, AUI/NRAO and NAOJ. The National Radio Astronomy Observatory is a facility of the National Science Foundation operated under cooperative agreement by Associated Universities, Inc.

REFERENCES

- | | |
|--|---|
| <p>Bannister, M. T., Kavelaars, J. J., Petit, J.-M., et al. 2016, <i>AJ</i>, 152, 70</p> <p>Barman, T. S., Macintosh, B., Konopacky, Q. M., & Marois, C. 2011, <i>ApJ</i>, 733, 65</p> | <p>Barman, T. S., Konopacky, Q. M., Macintosh, B., & Marois, C. 2015, <i>ApJ</i>, 804, 61</p> <p>Bonnefoy, M., Zurlo, A., Baudino, J. L., et al. 2016, <i>A&A</i>, 587, A58</p> |
|--|---|

- Booth, M., Jordán, A., Casassus, S., et al. 2016, *MNRAS*, 460, L10
- Bowler, B. P. 2016, *PASP*, 128, 102001
- Chiang, E., Kite, E., Kalas, P., Graham, J. R., & Clampin, M. 2009, *ApJ*, 693, 734
- Currie, T., Fukagawa, M., Thalmann, C., Matsumura, S., & Plavchan, P. 2012, *ApJ*, 755, L34
- Dohnanyi, J. S. 1969, *JGR*, 74, 2531
- Draine, B. T. 2006, *ApJ*, 636, 1114
- Esposito, S., Mesa, D., Skemer, A., et al. 2013, *A&A*, 549, A52
- Fabrycky, D. C., & Murray-Clay, R. A. 2010, *ApJ*, 710, 1408
- Foreman-Mackey, D., Hogg, D. W., Lang, D., & Goodman, J. 2013, *PASP*, 125, 306
- Gelman, A., Carlin, J. B., Stern, H. S., et al. 2014, *Bayesian data analysis*, Vol. 2 (CRC press Boca Raton, FL)
- Goździewski, K., & Migaszewski, C. 2014, *MNRAS*, 440, 3140
- Götberg, Y., Davies, M. B., Mustill, A. J., Johansen, A., & Church, R. P. 2016, *A&A*, 592, A147
- Gray, R. O., & Kaye, A. B. 1999, *AJ*, 118, 2993
- Holland, W. S., Matthews, B. C., Kennedy, G. M., et al. 2017, *MNRAS*, 470, 3606
- Hughes, A. M., Wilner, D. J., Andrews, S. M., et al. 2011, *ApJ*, 740, 38
- Ingraham, P., Marley, M. S., Saumon, D., et al. 2014, *ApJ*, 794, L15
- Kennedy, G. M., & Wyatt, M. C. 2010, *MNRAS*, 405, 1253
- Kenyon, S. J., & Bromley, B. C. 2002, *ApJ*, 577, L35
- Konopacky, Q. M., Barman, T. S., Macintosh, B. A., & Marois, C. 2013, *Science*, 339, 1398
- Konopacky, Q. M., Marois, C., Macintosh, B. A., et al. 2016, *AJ*, 152, 28
- Kratter, K. M., Murray-Clay, R. A., & Youdin, A. N. 2010, *ApJ*, 710, 1375
- Krivov, A. V., Löhne, T., & Sremčević, M. 2006, *A&A*, 455, 509
- MacGregor, M. A., Wilner, D. J., Rosenfeld, K. A., et al. 2013, *ApJ*, 762, L21
- MacGregor, M. A., Wilner, D. J., Andrews, S. M., Lestrade, J.-F., & Maddison, S. 2015, *ApJ*, 809, 47
- MacGregor, M. A., Wilner, D. J., Chandler, C., et al. 2016, *ApJ*, 823, 79
- Maire, A.-L., Skemer, A. J., Hinz, P. M., et al. 2015, *A&A*, 576, A133
- Malhotra, R. 1998, *Solar System Formation and Evolution*, ASP Conference Series, 149, 37
- Malo, L., Doyon, R., Lafrenière, D., et al. 2013, *ApJ*, 762, 88
- Marleau, G.-D., & Cumming, A. 2014, *MNRAS*, 437, 1378
- Marley, M.S., Fortney, J.J., Hubickyj, O., Bodenheimer, P., Lissauer, J.J. 2007, *ApJ*, 655, 541
- Marley, M. S., Saumon, D., Cushing, M., et al. 2012, *ApJ*, 754, 135
- Marois, C., Macintosh, B., Barman, T., et al. 2008, *Science*, 322, 1348
- Marois, C., Zuckerman, B., Konopacky, Q. M., Macintosh, B., & Barman, T. 2010, *Nature*, 468, 1080
- Matthews, B., Kennedy, G., Sibthorpe, B., et al. 2014, *ApJ*, 780, 97
- Moór, A., Kóspál, Á., Ábrahám, P., et al. 2015, *MNRAS*, 447, 577
- Mordasini, C. 2013, *A&A*, 558, A113
- Mustill, A. J., & Wyatt, M. C. 2009, *MNRAS*, 399, 1403
- Mustill, A. J., & Wyatt, M. C. 2012, *MNRAS*, 419, 3074
- Pan, M., & Sari, R. 2005, *Icarus*, 173, 342
- Pan, M., & Schlichting, H. E. 2012, *ApJ*, 747, 113
- Patience, J., Bulger, J., King, R. R., et al. 2011, *A&A*, 531, L17
- Pearce, T. D., & Wyatt, M. C. 2014, *MNRAS*, 443, 2541
- Pueyo, L., Soummer, R., Hoffmann, J., et al. 2015, *ApJ*, 803, 31
- Quillen, A. C. 2006, *MNRAS*, 372, L14
- Quillen, A. C., & Faber, P. 2006, *MNRAS*, 373, 1245
- Regaly, Z., Dencs, Z., Moor, A., & Kovacs, T. 2017, *arXiv:1710.01524*
- Reidemeister, M., Krivov, A. V., Schmidt, T. O. B., et al. 2009, *A&A*, 503, 247
- Ricci, L., Testi, L., Maddison, S. T., & Wilner, D. J. 2012, *A&A*, 539, L6
- Ricci, L., Carpenter, J. M., Fu, B., et al. 2015, *ApJ*, 798, 124
- Sadakane, K., & Nishida, M. 1986, *PASP*, 98, 685
- Schüppler, C., Löhne, T., Krivov, A. V., et al. 2015, *A&A*, 581, A97

- Soummer, R., Brendan Hagan, J., Pueyo, L., et al. 2011, ApJ, 741, 55
- Spiegel, D. S., & Burrows, A. 2012, ApJ, 745, 174
- Su, K. Y. L., Rieke, G. H., Stapelfeldt, K. R., et al. 2009, ApJ, 705, 314
- Su, K. Y. L., MacGregor, M. A., Booth, M., et al. 2017, AJ, 154, 225
- van Leeuwen, F. 2007, A&A, 474, 653
- Wertz, O., Absil, O., Gómez González, C. A., et al. 2017, A&A, 598, A83
- Williams, J. P., & Andrews, S. M. 2006, ApJ, 653, 1480
- Wilner, D. J., Andrews, S. M., & Hughes, A. M. 2011, ApJ, 727, L42
- Wisdom, J. 1980, AJ, 85, 1122
- Wright, D. J., Chené, A.-N., De Cat, P., et al. 2011, ApJ, 728, L20
- Wyatt, M. C. 2006, ApJ, 639, 1153
- Wyatt, M. C. 2008, ARAA, 46, 339
- Zurlo, A., Vigan, A., Galicher, R., et al. 2016, A&A, 587, A57